ChemPubSoc Europe

DOI: 10.1002/celc.201402378

CHEMELECTROCHEM Articles

Carboxyl Multiwalled Carbon-Nanotube-Stabilized Palladium Nanocatalysts toward Improved Methanol Oxidation Reaction

Yiran Wang,[a] Qingliang He,[a, b] Jiang Guo,[a] Huige Wei,[a] Keqiang Ding,*[c] Hongfei Lin,*[d] Saheel Bhana,[e] Xiaohua Huang,[e] Zhiping Luo,[f] T. D. Shen,[g] Suying Wei,*[a, b] and Zhanhu Guo*[a]

Carboxyl-functionalized multiwalled carbon nanotubes (MWNT-COOH) decorated with palladium (Pd) nanoparticles (NPs, Pd–MWNT-COOH) are prepared by using a one-pot thermal decomposition method without addition of reductant or surfactant. An increased ratio of the D band to G band in Raman spectra and a decreased ratio of oxygen-containing groups measured using X-ray photoelectron spectroscopy suggest the interaction between Pd NPs and carboxyl groups in Pd–MWNT-COOH. TEM studies reveal improved dispersion of Pd NPs after introducing MWNT-COOH or MWNTs; the carboxyl groups act as anchors to perfectly disperse Pd NPs in Pd–MWNT-COOH, which is responsible for the highest peak current of Pd–MWNT-COOH for the methanol oxidation reaction. The best catalytic performance is observed in conditions that afford a balanced adsorption between hydroxide and methanol through varying the concentrations of methanol and KOH. Increasing temperature can also improve the catalyst performance due to enhanced reaction kinetics.

1. Introduction

Nanoscale palladium (Pd) has drawn ever-increasing interest due to its unique catalytic, optical, electronic and plasmonic properties.[1] Pd-based nanocatalysts are not only widely applied in industrial areas including automobile catalytic converters and various hydrogenation reactions,[2] and also attract a great deal of scientific attention due to their catalytic sensitivity to size, shape and surrounding media.[3] Three typical synthesis methods including chemical reduction, thermal decomposition and electrochemical reduction have been used to synthesize Pd nanostructures with various morphologies such as nanocube,[4] nanorod,[5] nanowire,[6] hollow,[7] polyhedral,[8] dendrite,[9] nanoplate,[1b] porous nanotube,[10] tetrahexahedral[11] and nanourchin[12] structures. A well-known catalytic application of Pd nanoparticles (NPs) is direct methanol fuel cells (DMFCs). DMFCs are environmentally friendly power sources for transportation as portable and stationary power supplies in vehicles, auxiliary power units, and combined heat and power units.[13] Although platinum (Pt) is the best catalyst for the methanol oxidation reaction (MOR),[14] it is readily poisoned by the CO intermediates produced in acidic medium.[15] Pd, as a suitable low-cost catalyst, shows an increased CO tolerance in alkaline electrolyte, and thus provides an alternative for MOR.[16]

Unfortunately, tailoring of particle size and exploitation of NPs are often limited by aggregation of naked Pd NPs.[17] To overcome this problem, solid supporting substrates including carbon,[18] titania,[19] hydroxyapatite,[20] natural and artificial polymers,[21] polypyrrole,[22] and alumina[23] have been introduced to immobilize Pd NPs. Anchored on these substrates, the largely enhanced specific activity of Pd NPs makes low-loading catalysts practical for fuel cell operation. Among these promising catalyst-supporting materials, carbon materials such as carbon nanotubes (CNTs) have attracted interest due to their excellent electronic properties, good physicochemical stability, and large specific surface area.[24] Numerous methodologies have been reported for decorating CNTs with Pd NPs, in-

[a] Y. Wang,[+] Q. He,[+] J. Guo, H. Wei, Prof. S. Wei, Prof. Z. Guo
Integrated Composites Laboratory (ICL)
Dan F. Smith Department of Chemical Engineering
Lamar University, Beaumont, TX 77710 (USA)
E-mail: zguo10@utk.edu

[b] Q. He,[+] Prof. S. Wei
Department of Chemistry and Biochemistry
Lamar University, Beaumont, TX 77710 (USA)
E-mail: suying.wei@lamar.edu

[c] Prof. K. Ding
College of Chemistry and Materials Science
Hebei Normal University, Shijiazhuang, 050024 (China)
E-mail: dkeqiang@263.net

[d] Prof. H. Lin
Chemical and Materials Engineering Department
University of Nevada, Reno, NV 89557 (USA)
E-mail: hongfeil@unr.edu

[e] S. Bhana, Prof. X. Huang
Department of Chemistry and Bioinformatics Program
The University of Memphis, Memphis, TN 38152 (USA)

[f] Prof. Z. Luo
Department of Chemistry and Physics
Fayetteville State University, Fayetteville, NC 28301 (USA)

[g] Prof. T. D. Shen
State Key Laboratory of Metastable Materials Science and Technology
Yanshan University, Hebei, 066004 (China)

[+] These authors contributed equally to the work

© 2015 Wiley-VCH Verlag GmbH & Co. KGaA, Weinheim

cluding vapor deposition,[25] in situ chemical,[26] impregnation,[27] plasma,[28] and electrochemical methods.[29] Overall, Pd–CNTs nanocatalysts can be synthesized in two ways. The first is to directly load the Pd NPs on the CNTs through van der Waals interactions. However, the adhesion between NPs and CNTs is poor, leading to fast degradation and poor cycle performance of the catalysts. The second method—by growing Pd NPs on the CNTs via covalent bonding—is an effective way to obtain highly stable Pd–CNTs. However, as CNTs are chemically inert and hydrophobic in nature, it is critical to activate their surface for controlled functionality. Among many functional groups, carboxyl groups are commonly used as nucleation sites for the deposition of metal NPs by acting as anchors for the growth of metal NPs, thus favoring the formation of highly dispersed and stable composite materials.[30] In parallel, metal acetylacetonates have become alternatives to metal chloride and nitrate precursors for the preparation of supported metal catalysts by thermal decomposition in organic solvents, which excluding the addition of reductant.[31] Furthermore, the surfactants and coordinating ligands typically used to control the size and distribution inevitably affect the metal properties.[32] To the best of our knowledge, direct decomposition of palladium acetylacetonate [$Pd(acac)_2$] in the presence of carboxyl-functionalized multiwalled carbon nanotubes (MWNT-COOH) without the addition of reducing reagents or surfactants has not been reported for the preparation of Pd nanocatalysts.

In this work, a one-pot solution-based method was introduced to synthesize MWNT-COOH-stabilized Pd nanocatalysts (Pd–MWNT-COOH). A facile, in situ thermal decomposition of $Pd(acac)_2$ in a solution of MWNT-COOH in xylene at reflux was used, in which highly dispersed palladium Pd NPs were strongly anchored to the MWNT-COOH surface. Bare Pd and Pd NPs anchored on MWNT without surface carboxyl groups were also synthesized for comparison. The crystalline structure and morphology of the Pd NPs were investigated by X-ray diffraction (XRD) and transmission electron microscopy (TEM). The variation in defects of the nanotubes was characterized by Raman spectroscopy. The thermal properties and final Pd loading of the synthesized nanocatalysts were determined by thermogravimetric analysis (TGA). The composition and synthesis mechanism of the nanocatalysts were investigated by X-ray photoelectron spectroscopy (XPS). The electrocatalytic performances of bare Pd NPs, Pd–MWNT, and Pd–MWNT-COOH toward MOR were compared using cyclic voltammetry (CV), chronoamperometry (CA), and electrochemical impedance spectroscopy (EIS). The effects of both the methanol and alkaline concentrations, and the temperature (2–40 °C) on the Pd–MWNT-COOH nanocatalyst for MOR were also investigated using CV, CA, and Tafel polarization.

2. Results and Discussion

2.1. Characterizations of Nanocatalysts

2.1.1. XRD Analysis

Figure 1a–e shows the XRD patterns of the as-received MWNT-COOH, Pd–MWNT-COOH, as-received MWNTs, Pd/MWNTs and bare Pd NPs. For MWNT-COOH and MWNTs (Figure 1a and c), a main diffraction peak centered at around 26° was observed assigned to the (002) facet of MWNTs (JCPDS card, 26–1077). For Pd–MWNT and Pd–MWNT-COOH (Figure 1b and d), three characteristic peaks corresponding to the (111), (200) and (220) facets of the face-centered cubic (fcc) crystalline Pd, as well as the main diffraction peak of MWNTs, were observed, suggesting the successful deposition of Pd NPs on the MWNTs and MWNT-COOH. The only diffraction peaks of Pd observed for bare Pd NPs (Figure 1e), indicate the formation of Pd NPs by direct thermal decomposition of $Pd(acac)_2$, which is consistent with the previously reported synthesis of Pd NPs by the chemical reduction method.[33] In addition, the C(002) facet is found to be suppressed significantly after the deposition of Pd NPs, which might be caused by the strong signal of Pd NPs.

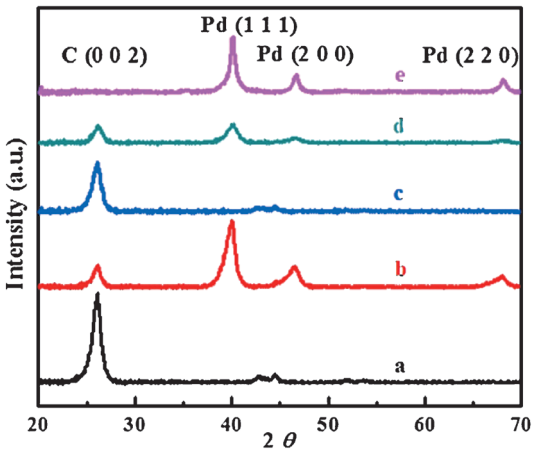

Figure 1. XRD patterns of a) MWNT-COOH, b) Pd–MWNT-COOH, c) MWNTs, d) Pd–MWNTs, and e) bare Pd NPs.

2.1.2. Microstructure Investigation

The TEM microstructures of the bare Pd NPs, Pd–MWNT and Pd–MWNT-COOH are shown in Figure 2a–c, together with the histogram (top inset) and HRTEM (bottom inset) of the corresponding nanocatalysts. The selected area electron diffraction (SAED) pattern for each nanocatalyst is also shown. Although bare Pd NPs are produced by simple thermal decomposition of $Pd(acac)_2$, serious agglomeration is observed (Figure 2a). Using the MWNTs and MWNT-COOH as solid supports, the Pd NPs are more uniformly distributed than the bare Pd NPs (Figure 2b and c). However, for the Pd–MWNTs, poor deposition with slight agglomeration was observed and the distribution of Pd NPs is less uniform than that on the MWNT-COOH. The Pd NPs were observed to be decorated on the MWNT-COOH with an excellent distribution. The average particle size of Pd NPs, obtained from the histograms, is 6.27, 2.88 and 10.14 nm for the bare Pd NPs, Pd–MWNTs and Pd–MWNT-COOH, respectively. In addition, it is clear from the histograms (Figure 2a–c, inset) that Pd NPs exhibit a sharp distribution in Pd–MWNT-COOH compared to Pd–MWNTs, indicating a dispersal role for the COOH groups. Both Pd(111, 200, 220, and 311) and PdO(112) were observed in all SAED patterns, consistent with the XRD

© 2015 Wiley-VCH Verlag GmbH & Co. KGaA, Weinheim

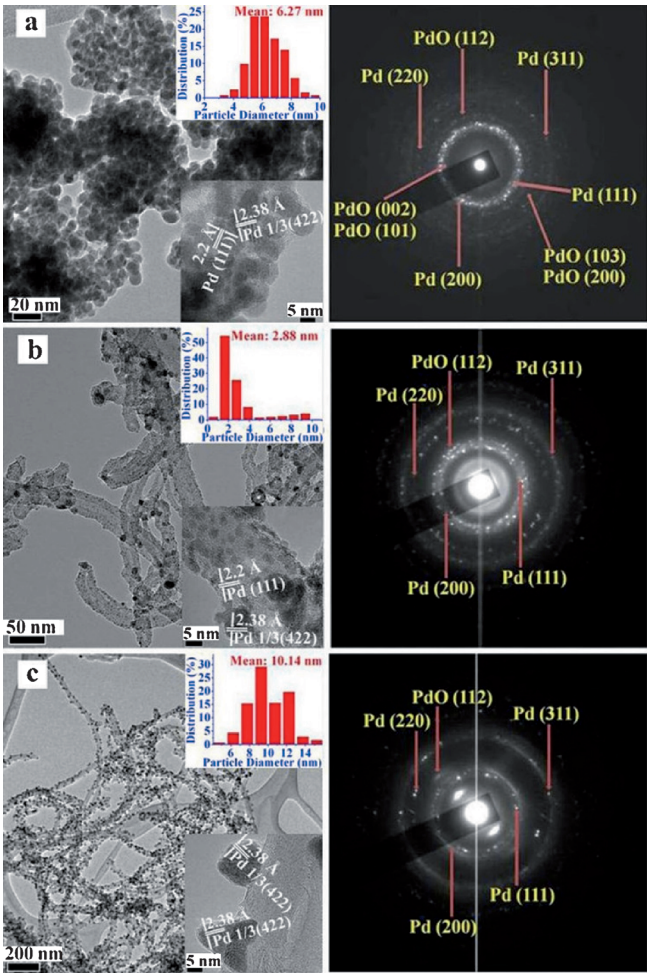

Figure 2. TEM microstructures of a) bare Pd NPs, b) Pd–MWNTs, and c) Pd–MWNT-COOH. Inset: particle-size histograms (top) and HRTEM images (bottom) of the corresponding nanocatalysts. The HRTEM images provide a closer view of the lattice fringes of the Pd NPs. Beside each TEM is the corresponding SAED pattern.

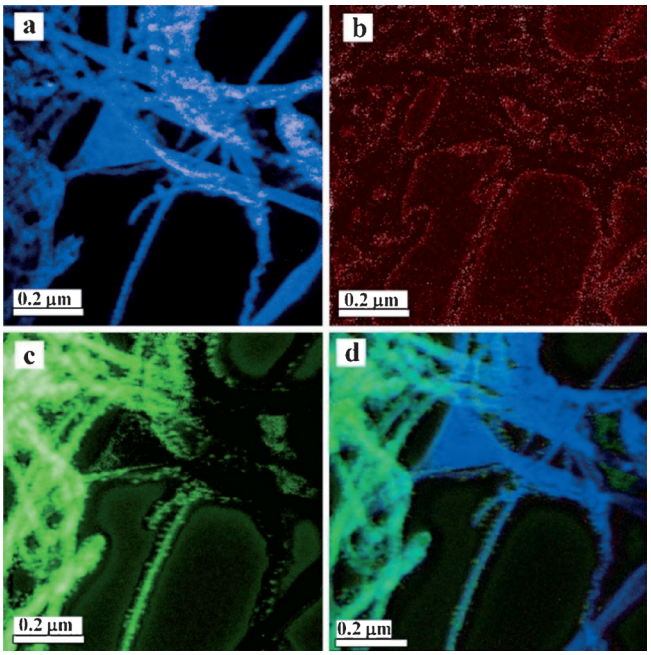

Figure 3. EFTEM of Pd–MWNT-COOH. a) C, b) O, c) Pd, and d) C + O + Pd map.

results of Pd and the subsequent XPS analysis of Pd^{2+}. The inset of Figure 2a–c shows the HRTEM microstructures of the bare Pd NPs, Pd–MWNTs and Pd–MWNT-COOH. The Pd NPs were observed to be embedded on the MWNT-COOH, implying a strong chemical interaction between the Pd NPs and MWNT-COOH with the reported anchoring role of the carboxyl groups.[34] In contrast, ultrafine Pd NPs were observed to attach on the tube wall due to the absence of anchors, which play a nucleation role in the growth of Pd NPs as confirmed by the large Pd particle size in Pd–MWNT-COOH. The clear lattice fringe of about 0.22 nm observed by HRTEM belongs to the (111) plane of fcc Pd, and is consistent with the spacing (0.238 nm) of fringes due to the kinetically forbidden reflections of Pd 1/3(422), which is expected to appear in thin films or platelets with (111) surfaces.[35]

Energy-filtered TEM (EFTEM) was used to identify the 2D elemental distribution. The elemental maps of C, O, Pd, and C + O + Pd are shown in Figure 3. The elements are shown with different colors (red: O, blue: C, green: Pd). Brighter areas of the elemental map indicate higher concentrations of the corresponding element in that area. Figure 3a shows the carbon map, in which the nanotubes and the lacey carbon grid of TEM are both blue. The red coverage in Figure 3b suggests that the oxygen is contained in the synthesized Pd–MWNT-COOH, which is also consistent with the SAED results. The map in Figure 3c shows that Pd is evenly distributed on the support. The overlay (Figure 3d) shows the even distribution of Pd (green dots) on the carbon nanotubes (blue), together with the coverage of O (red). These results suggest the containment of Pd, O and C and further confirm the uniform distribution of the Pd NPs on MWNT-COOH.

2.1.3. Raman Analysis

In order to evaluate the change of structural perturbation of the nanotubes, the Raman characterization technique was chosen because of its high sensitivity to the crystallinity of the nanotube surface.[36] The Raman spectra of MWNT-COOH, Pd–MWNT-COOH, MWNTs, Pd–MWNTs and bare Pd NPs in the spectral range 1000–1800 cm^{-1} are shown in Figure 4a–e. These MWNT-based nanocatalysts display similar characteristic peaks. The peak at 1309 cm^{-1} is a "dispersive" band (also called the D band) arising from the defect sites.[37] The high-frequency peak at 1605 cm^{-1} is close to that observed for well-ordered graphite (known as the G band), which is universal to all carbon structures having sp^2 hybridization. Due to the curvature of the CNTs, in contrast to the perfect honeycomb lattice of graphite, the G band is split into the G^- and G^+ bands centered around 1576 and 1604 cm^{-1}, respectively.[38] The intensity ratio of D to G bands (I_D/I_G) provides information about the degree of structural defects on the tube wall surface and has been considered as a probe of the degree of functionalization

© 2015 Wiley-VCH Verlag GmbH & Co. KGaA, Weinheim

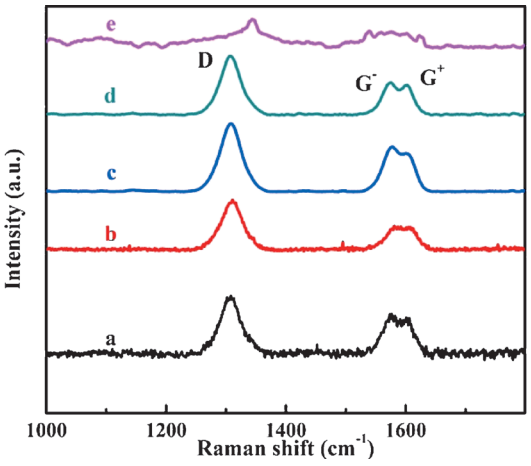

Figure 4. Raman spectra, showing the D and G bands, of a) MWNT-COOH, b) Pd–MWNT-COOH, c) MWNTs, d) Pd–MWNTs, and e) bare Pd NPs.

on the tube walls.[39] The higher the I_D/I_G value, the larger the degree of functionalization.[40] On the one hand, it was calculated from the Raman spectrum that both increases were apparent in the I_D/I_G values for the Pd–MWNT-COOH (1.85) versus pure MWNT-COOH (1.52), and Pd–MWNTs (2.11) versus pure MWNTs (1.43) after the deposition of Pd NPs. On the other hand, a slight increase of I_D/I_G in MWNT-COOH compared with MWNTs was observed, suggesting that the functionalization of carboxyl groups increases the number of defects on the tube wall. In addition, similar D and G bands were also observed for bare Pd NPs, which could be attributed to the excess acac ($I_D/I_G = 1.89$). The increased I_D/I_G value after deposition of Pd NPs might be due in part to the excess acac on the Pd NP surface. Finally, the NPs deposited on the tube wall surface will also give rise to more structural defects, thus increasing I_D/I_G.[41]

2.1.4. XPS Analysis

XPS is a powerful tool to provide valuable insights into the surface of solid samples, that is, to identify the atomic composition of solid surfaces and to determine their local chemical environments. In particular, the valence state of elements can be determined based on the specific binding energy measured from a corresponding type of photoelectron.[42] Figure 5a shows the wide-scan survey spectrum of the synthesized Pd–MWNT-COOH over the range 0–1000 eV. Four main spectral peaks were observed at approximately 279.14, 330.15, 527.84, and 561.04 eV and correspond to C 1s, Pd 3d, O 1s, and Pd 3p emissions, respectively.[43] The wide-scan survey also confirmed the aforementioned EFTEM results.

The high-resolution XPS spectrum was used to confirm the Pd valence state. Figure 5b shows the Pd 3d spectra of Pd–MWNT-COOH after peak deconvolution. The XPS spectrum of the Pd 3d level is curve-fitted with two spin-orbit-split doublets corresponding to Pd $3d_{3/2}$ and Pd $3d_{5/2}$ components. The peaks at 335.32 and 340.66 eV correspond to the orbits of metallic Pd $3d_{5/2}$ and Pd $3d_{3/2}$, respectively. For Pd^{2+}, the binding energy peaks at 337.39 and 342.75 eV belong to the Pd $3d_{5/2}$ and Pd $3d_{3/2}$ orbits.[44] It is confirmed that the Pd^{2+} in the synthesized nanocatalysts are probably due to the incomplete decomposition of $Pd(acac)_2$. The initial and final peak positions of Pd^0 $3d_{5/2}$, Pd^0 $3d_{3/2}$, Pd^{II} $3d_{5/2}$ and Pd^{II} $3d_{3/2}$ are summarized in Table 1. All the characteristic peaks shift positively in the synthesized Pd–MWNT-COOH nanocatalysts, suggesting an interaction between the Pd NPs and the MWNT-COOH.[45] From the peak areas listed in Table 1, the Pd/PdO mass ratio was calculated to be 1.74 :1.

High-resolution C 1s XPS spectra of the as-received MWNT-COOH and the synthesized Pd–MWNT-COOH are shown in Figure 5c and d. The C 1s peak of MWNT-COOH can be smoothly deconvoluted into four fitting curves with peaks at 284.8, 286.6, 288.2 and 290.1 eV, which correspond to C–C, C–O,

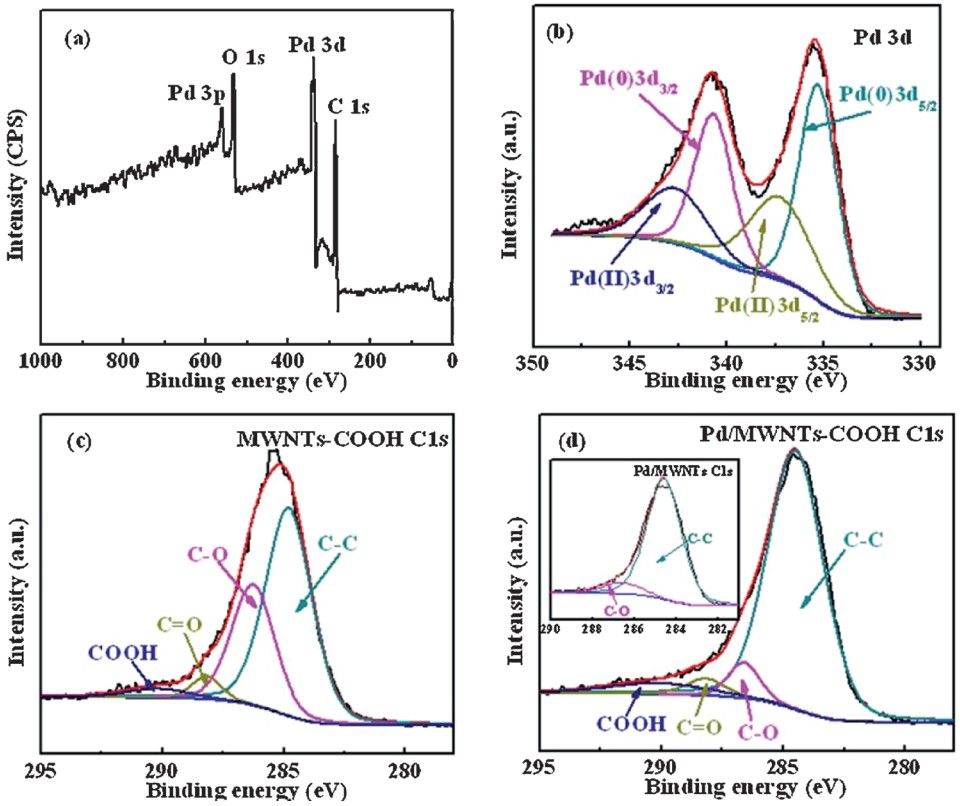

Figure 5. XPS spectra of Pd–MWNT-COOH: a) wide-scan survey, b) curve fit of Pd 3d, c) curve fit of C 1s, and d) curve fit of C 1s; inset: curve fit of the C 1s in Pd–MWNTs.

© 2015 Wiley-VCH Verlag GmbH & Co. KGaA, Weinheim

Table 1. Original and final positions of Pd 3d binding energies for Pd and Pd^{2+} in the Pd–MWNT-COOH nanocatalysts, and calculated area of the binding energy peaks.

Peak	Original position [eV]	Position [eV]	Area
Pd $3d_{5/2}$ (metal)	334.72	335.32	26878.2
Pd $3d_{3/2}$ (metal)	340.35	340.66	17918.8
Pd $3d_{5/2}$ (PdO)	336.16	337.39	15459.23
Pd $3d_{3/2}$ (PdO)	341.23	342.75	10306.15

C=O, and O–C=O, respectively.[46] The O–C=O peak demonstrates the presence of carboxyl groups in MWNT-COOH. The deconvolution of the C 1s curve for the synthesized Pd–MWNT-COOH (Figure 5d) is almost the same as that for MWNT-COOH, suggesting that the deposition of Pd NPs on the tube wall surface has not changed the chemical structures of MWNTs. However, the observed decrease of oxygen-containing groups indicates the binding of functionalized groups with Pd NPs. In contrast, only two peaks corresponding to C–C and C–O are observed in the high-resolution C 1s XPS spectra of Pd–MWNTs due to the relatively fewer defects (Figure 5d, inset). Therefore, the strong anchoring of Pd NPs could take place, with the carboxyl groups on the MWNT-COOH surface acting as nucleation sites; the carboxyl groups bind the Pd NPs tightly due to the bonding interaction with the C=O.[47]

2.1.5. Thermogravimetric Analysis

Figure 6a–f shows the TGA curves of $Pd(acac)_2$, bare Pd NPs, MWNTs, Pd–MWNTs, MWNT-COOH and Pd–MWNT-COOH in air at 30–800 °C. For $Pd(acac)_2$ (Figure 6a), a sharp decrease of weight loss is observed up to 200 °C, which corresponds with the melting point of $Pd(acac)_2$ (200–251 °C). After the total loss of acac up to 260 °C, the curve shows a slight increase in weight due to the oxidation of Pd NPs and the final residue, at 28.15%, is approximately consistent with the molecular weight percentage of Pd in $Pd(acac)_2$. For bare Pd NPs (Figure 6b), similar weight loss trends up to 200 °C, and a subsequent small weight increase were observed due to the loss of acac on the Pd surface and the oxidation of Pd. The Pd loading, calculated from the final PdO residue, was 57.54%. For MWNTs and MWNT-COOH (Figure 6c and e), both sharp decreases are observed due to the burning of carbon at 500 °C. However, a slight weight loss in MWNT-COOH was observed in the range 200–400 °C and is probably due to the decomposition of COOH. For Pd–MWNTs and Pd–MWNT-COOH (Figure 6d and f), the decomposition of acac and oxidation of Pd contributed to the slight weight decrease and subsequent weight increase in the range 200–300 °C. Finally, the Pd–MWNTs and Pd–MWNT-COOH nanocatalysts remain as a constant residue after the burning of MWNTs. The percentages of the final residue as PdO were 34.3 and 46.91% for Pd–MWNTs and Pd–MWNT-COOH nanocatalysts, respectively, and the total loadings of Pd in Pd–MWNTs and Pd–MWNT-COOH were calculated to be 32.46 and 44.12%, respectively. The higher loading of Pd in Pd–MWNT-COOH than in Pd–MWNTs further confirms the inert nature of MWNTs and the anchoring role of carboxyl groups on MWNTs that can facilitate a higher Pd loading.

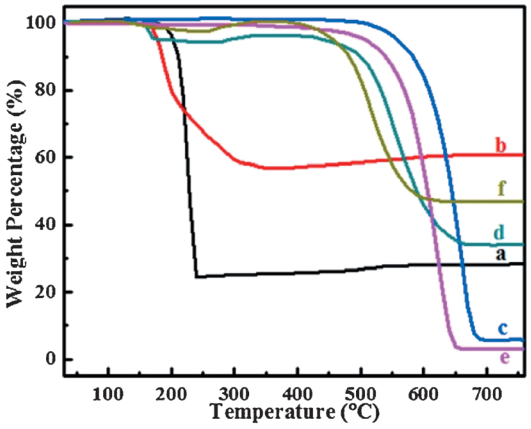

Figure 6. TGA curves of a) $Pd(acac)_2$, b) bare Pd NPs, c) MWNTs, d) Pd–MWNTs, e) MWNT-COOH, and f) Pd–MWNT-COOH.

2.1.6. Mechanism of Formation of Pd–MWNT-COOH Nanocatalysts

The decomposition of $Pd(acac)_2$ to Pd atoms has been reported with the formation of acetylacetonate.[48] In xylene heated at reflux, CO molecules are proposed to be generated in situ from the decomposition of acetylacetonate[48a] and act as reductants for the formation of Pd NPs. During the decomposition process, the produced Pd atoms first form clusters, which are evenly distributed on the surface of MWNT-COOH through their interaction with C=O functional groups.[47] The growth proceeds as more Pd atoms are deposited around these nuclei to form Pd NPs. The carboxyl groups on the surface of the nanotubes act as the capping head to tightly bind the elemental Pd formed in situ and the subsequently formed Pd NPs. One may conclude that the Pd NPs can be evenly distributed and firmly embedded on the surface of MWNT-COOH through chemical bonding. The formation is shown in Scheme 1.

2.2. Electrocatalytic Behavior

2.2.1. Electrocatalytic Evaluations toward MOR

CV is an important technique for the investigation of the electrocatalytic activity and to estimate the electrochemically active surface area (ECSA) of Pd-based catalysts. Not only is ECSA an important index related to the active sites of the catalyst, but it can also be used to assess the conductive pathways available for electron transfer from and to the catalyst surface.[49] Figure 7A and B show the cyclic voltammograms of bare Pd NPs, Pd–MWNTs, and Pd–MWNT-COOH in 1.0 M KOH and 1.0 M KOH containing 1.0 M methanol solutions at a scan rate of 50 mV s^{-1}, respectively. For all the nanocatalysts featured in Figure 7A, typical peaks are well defined as peak I: hydrogen oxidation; peak II: oxidative desorption of H and adsorption of OH^-; peak III: oxidation of Pd; peak IV: reduction of

© 2015 Wiley-VCH Verlag GmbH & Co. KGaA, Weinheim

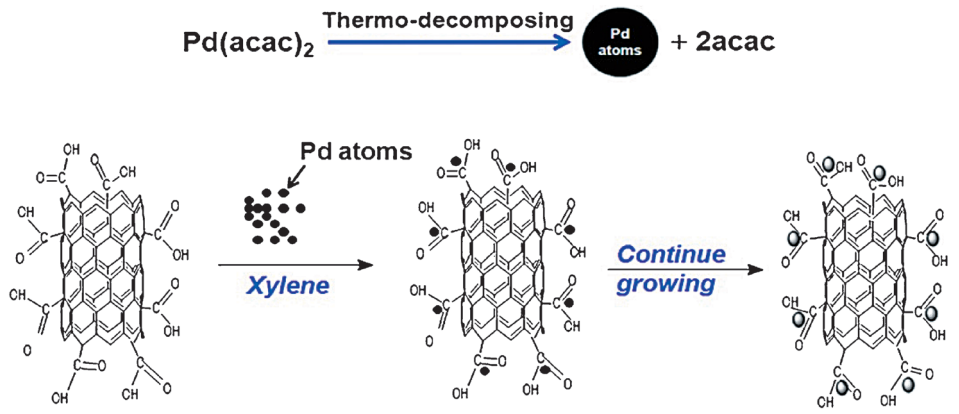

Scheme 1. Synthesis of MWNT-COOH-stabilized Pd nanocatalysts.

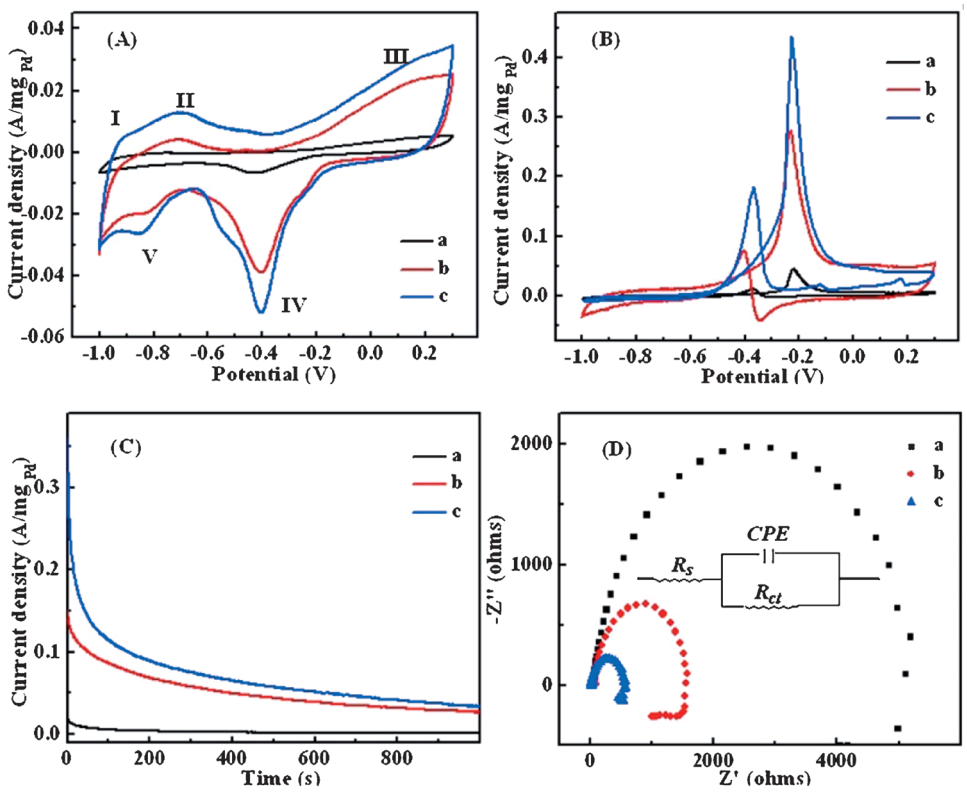

Figure 7. Electrochemical characterization of bare Pd NPs (a), Pd–MWNTs (b), and Pd–MWNT-COOH (c). CV in A) 1.0 M KOH and B) 1.0 M KOH containing 1.0 M methanol at a scan rate of 50 mV s^{-1} at room temperature. C) CA in 1.0 M KOH containing 1.0 M methanol for 1000 s at −0.25 V. D) EIS in 1.0 M KOH containing 1.0 M methanol at −0.4 V vs. SCE. Inset: equivalent circuit used to fit the impedance spectra.

Table 2. CV and EIS fitting results of nanocatalysts.

Nanocatalyst	ECSA [$m^2 g_{Pd}^{-1}$]	j [$A mg_{Pd}^{-1}$]	R_s [Ω]	R_{ct} [Ω]
Bare Pd NPs	8.83	0.046	44.93	4570
Pd–MWNTs	49.38	0.277	66.78	1401
Pd–MWNT-COOH	64.22	0.436	12.45	510.6

PdO; peak V: reductive adsorption/absorption of H.[50] The integral of peak IV is commonly used to estimate the ECSA based on the columbic charge for the reduction of PdO, according to Equation (1):[51]

$$ECSA = Q/SL \quad (1)$$

where Q is the charge associated with PdO stripping, S is te proportionality coefficient as 405 μC cm^{-2}, which is used to relate charges with peak area, assuming that a monolayer of PdO covers on surface, L is the Pd loading [g]. The estimated ESCAs are given in Table 2. It is clearly obtained that the ESCA values follow the order as Pd–MWNT-COOH > Pd–MWNTs > bare Pd NPs, due to the dispersive role of MWNT and the enhanced utilization of Pd NPs brought about by the COOH moieties. For the cyclic voltammograms of nanocatalysts toward MOR (Figure 7B), in the potential range −0.8 to −0.6 V, the oxidation of the absorbed and adsorbed hydrogen proceeds as Reaction (a):[52]

$$Pd - H_{ads} + OH^- \rightarrow Pd + H_2O + e^- \quad (a)$$

The reversible adsorption of methanol also occurs in this potential region in the presence of methanol [Reaction (b)]:[53]

$$Pd + CH_3OH_{sol} \leftrightarrow Pd - CH_3OH_{ads} \quad (b)$$

Following the dissociation–adsorption step, methanol begins to be oxidized, from −0.6 V with continual increase of the current, and a current peak centered at −0.2 V was observed during the forward scan. The corresponding oxidation processes are described by Reactions (c–h):[54]

$$Pd - CH_3OH_{ads} + OH^- \rightarrow Pd - CH_3O_{ads} + H_2O + e^- \quad (c)$$

$$Pd - CH_3O_{ads} + OH^- \rightarrow Pd - CH_2O_{ads} + H_2O + e^- \quad (d)$$

© 2015 Wiley-VCH Verlag GmbH & Co. KGaA, Weinheim

$$Pd - CH_2O_{ads} + OH^- \rightarrow Pd - CHO_{ads} + H_2O + e^- \quad (e)$$

$$Pd - CHO_{ads} + OH^- \rightarrow Pd - CO_{ads} + H_2O + e^- \quad (f)$$

$$Pd - CO_{ads} + OH^- \rightarrow Pd - COOH_{ads} + e^- \quad (g)$$

$$Pd - COOH_{ads} + OH^- \rightarrow Pd + CO_2 + H_2O + e^- \quad (h)$$

The current begins to decrease with further increase of the potential due to the increased coverage of the CO_{ads} intermediates on the Pd active sites.[55] Furthermore, the depletion of methanol near the electrode surface is another reason for the decrease in current.[56] Finally, the formation of metal oxide at higher potentials also reduces the number of Pd active sites, which contribute to a decreased current [Reactions (i–k)]:[52]

$$Pd + OH^- \rightarrow Pd - OH_{ads} + e^- \quad (i)$$

$$Pd - OH_{ads} + OH^- \rightarrow PdO + H_2O + e^- \quad (j)$$

$$Pd - OH_{ads} + Pd - OH_{ads} \rightarrow PdO + H_2O \quad (k)$$

During the negative scan, the electrode surface is reactivated by reducing Pd^{II} oxide—evidenced by the presence of another peak at approximately −0.4 V—giving rise to a re-oxidation peak that is primarily a result of the removal of incompletely oxidized carbonaceous species formed during the forward scan.[15] The peak current density (j_p) of bare Pd NPs, Pd–MWNTs and Pd–MWNT-COOH are shown in Table 2. The j_p values of Pd–MWNT-COOH and Pd–MWNTs are higher than that of bare Pd NPs, suggesting that the catalytic activity of Pd NPs can be greatly improved by using MWNTs and MWNT-COOH as supports. In addition, the j_p value of Pd–MWNT-COOH was also observed to be much higher than that of Pd–MWNTs, demonstrating the positive role of carboxyl groups on MWNTs in facilitating Pd deposition, by contributing to the uniform distribution of Pd NPs and promoting a strong interaction between Pd NPs and MWNT-COOH.

In order to further probe the tolerance of these three nanocatalysts toward intermediate carbonaceous species, CA measurements were performed in 1.0 M aqueous KOH containing 1.0 M methanol for a duration of 1000 s. Figure 7C shows the CA curves at −0.25 V; these three were observed to be similar results, as all the polarization currents decreased rapidly during the initial period, then gradually, the current decayed and a pseudo-steady state was achieved. The decrease in current is due to surface poisoning induced by the CO_{ads} species. Among the synthesized nanocatalysts in this study, Pd–MWNT-COOH was able to maintain a relatively low decaying rate. The observed highest extreme current indicates the best electrocatalytic stability, which is probably due to the strong interaction between Pd NPs and MWNT-COOH.

EIS—a sensitive electrochemical technique for the study of electrooxidation kinetics—was also conducted in 1.0 M KOH solution containing 1.0 M methanol at −0.4 V versus SCE.[57] Figure 7D shows the semicircular Nyquist plots of imaginary Z'' [Ω] versus real Z' [Ω] components of impedance of these three nanocatalysts. The semicircular plots indicate that the reactions are kinetically controlled and the diameter of the semicircle can be used to measure the charge-transfer resistance (R_{ct}) of the catalyst. A decrease in the diameter of the semicircular Nyquist plot always represents a decrease in the charge-transfer resistance and an enhancement of charge-transfer reaction kinetics, which is an evaluation of how fast the charge transfer is during the oxidation process.[58] The R_{ct} values of the nanocatalysts were estimated by fitting the EIS curves using the ZSimpWin software (Princeton Applied Rearch) based on an equivalent electric circuit (Figure 7D, inset). In this R_s (R_{ct} CPE) circuit, R_s represents the uncompensated solution resistance and the constant-phase element (CPE) is the frequency-dependent capacitance. The parallel combination of the charge-transfer resistance and CPE takes into account the thin electrode film and methanol adsorption and oxidation.[59] The parallel combination (R_{ct} CPE) leads to a depressed semicircle in the corresponding Nyquist impedance plot.[60] The values for the parameters R_s and R_{ct} are also summarized in Table 2. The R_s values are almost the same due to the same solution resistance, however, the R_{ct} of these three nanocatalysts follow the order Pd–MWNT-COOH > Pd–MWNTs > bare Pd NPs due to the positive role of the COOH group.

2.2.2. Effect of Methanol Concentration on MOR

Figure 8 shows the cyclic voltammograms of the MOR on the Pd–MWNT-COOH electrode in 1.0 M aqueous KOH solution containing different concentrations of methanol ranging from 1.0 to 25.0 M at a scan rate of 50 mV s^{-1}. The magnification of the onset potential region is shown inset. The cyclic voltammograms exhibit similar shapes to that in Figure 7B, that is, peak I for the oxidation of fresh methanol, and peak II for the re-oxidation of the carbonaceous species formed during the forward scan process. However, varying the methanol concentrations has an obvious effect on j_p. The j_p value initially increases with increasing methanol concentration, reaches a maximum at

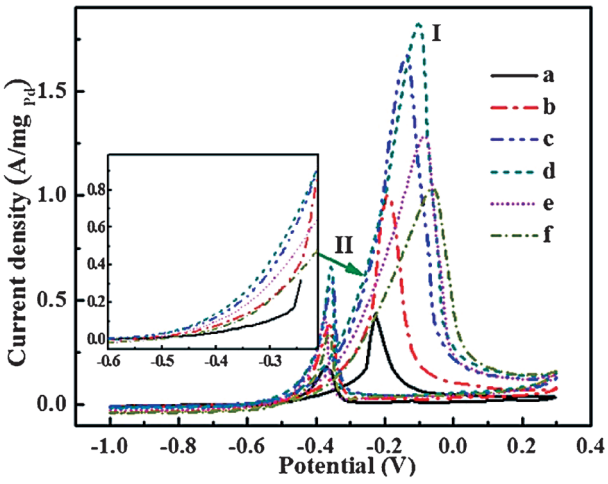

Figure 8. CV of the MOR at the Pd–MWNT-COOH electrode in 1.0 M KOH solution with methanol concentrations of a) 1.0, b) 6.0, c) 12.0, d) 16.0, e) 22.0, and f) 25.0 M, at a scan rate of 50 mV s^{-1} at room temperature. Inset: the magnification of the onset potential region.

© 2015 Wiley-VCH Verlag GmbH & Co. KGaA, Weinheim

12.0 M, and decreases with further increase in the methanol concentration. The variation of j_p is due to the amount of OH_{ads} that is not affected by methanol coverage in solutions with lower methanol concentrations. The j_p value increases greatly with increasing the methanol concentration due to the electron-donor role of methanol as indicated by Reactions (c–h).[61] However, the competition between the two adsorbed species (OH_{ads} vs. methanol) on the Pd–MWNT-COOH electrode becomes more significant with increasing methanol concentration. The adsorption of OH (OH_{ads}) will be hindered by the increased methanol adsorption at high potentials—insufficient coverage of the Pd–OH_{ads} will result in decreased j_p, according to Reactions (c–h). The excessive adsorbed reaction intermediates on the electrode will also cover the active sites of Pd and contribute further to the decrease of j_p.

In addition to the variation of j_p, a positive shift in peak potential (E_p), indicative of a harder process, was also observed at increased methanol concentrations. During the oxidation of methanol, greater amounts of intermediate species will accumulate on the active sites of Pd. The unoxidized organic residues will accumulate with increasing methanol concentration and require higher potential to oxidize them. Simultaneously, the increased coverage of poisoning species blocks the adsorption of OH^- and makes oxidation of methanol less favorable. In addition, the methanol oxidation peak was observed to broaden with increasing methanol concentration. The broadened peaks are due to the increased accumulated methanol intermediates on the catalyst surface, which require higher potential and longer time to be oxidized. This relationship between methanol concentration and E_p can be attributed to the IR drop originating from the internal resistance or equivalent series resistance.[62] Finally, the onset potentials were observed to vary consistently with j_p (Figure 8, inset), which further confirms the mechanism by which the highest current density is determined by a balance of coverage between OH_{ads} and methanol.

2.2.3. Effect of KOH Concentration on MOR

Figure 9 shows the cyclic voltammograms for MOR on the Pd–MWNT-COOH electrode in 12.0 M methanol solution that contains KOH at concentrations ranging from 0.1 to 4.0 M. The cyclic voltammograms were measured at a scan rate of 50 mV s^{-1} between −1.0 and 0.3 V at room temperature. Two clear phenomena were observed for the KOH concentration effect. On the one hand, the j_p value was observed to increase with increasing KOH concentration from 0.1 to 1.0 M; a further increase to 4.0 M led to an obviously decreased j_p value. In solutions with low KOH concentration, the adsorption of hydroxide is far from saturated, and is largely blocked by the adsorbed methanol molecules. An increased supply of hydroxide will therefore lead to an increased j_p value, due to the promoting function of OH_{ads}, in accordance with Reactions (c–h). However, with further increasing KOH concentration, the supply of hydroxide will be excessive and result in an excess coverage of OH_{ads} on the Pd; the dominating function of OH_{ads} on the electrode will block further adsorption of methanol and therefore,

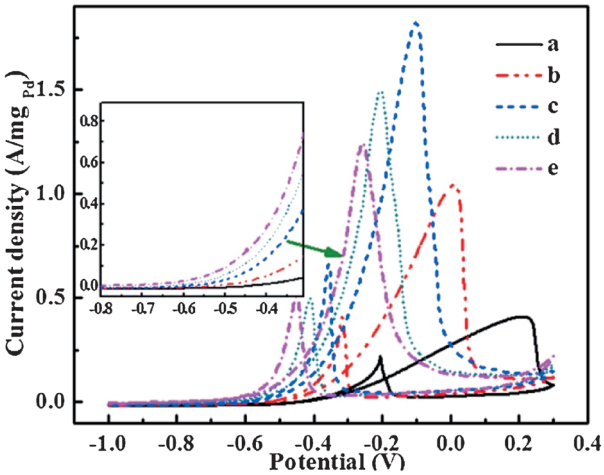

Figure 9. CV of the MOR at the Pd–MWNT-COOH electrode in solutions containing 12.0 M methanol with KOH concentrations of a) 0.1, b) 0.25, c) 1.0, d) 2.0, and e) 4.0 M, at a scan rate of 50 mV s^{-1} at room temperature. Inset: the magnification of the onset potential region.

as the coverage of methanol is insufficient, the absence of electron donor will lead to a decreased j_p. Furthermore, the increase in KOH concentration can also accelerate the formation of Pd^{II} oxides according to Reactions (i–k), which also contributes to decreased j_p values at higher potentials.

Simultaneously, different phenomena involving E_p have been observed to exhibit a continuous negative shift with increasing KOH concentration. The negative shift in E_p suggests that the increased KOH concentration has a favorable effect on the oxidation of methanol. In other words, the methanol oxidation occurs more readily and easily on the catalyst due to the increase of adsorbed OH^-. The negative shift of E_p can be understood, based on Reactions (c–h), as the dehydrogenation process. The increase of total OH^- in the solution will lead to a higher coverage of reactive Pd–OH_{ads}, facilitating the removal of the adsorbed intermediates. Furthermore, in the presence of sufficient OH^-, the oxidation of carbonaceous intermediates can proceed directly through Reactions (l) and (m), causing the negative shift of E_p:[53]

$$Pd - CH_xO_{ads} + x\,OH^- \rightarrow Pd - CO_{ads} + x\,H_2O + x\,e^- \quad (l)$$

$$Pd - CO_{ads} + 2\,OH^- \rightarrow Pd + CO_2 + H_2O + 2\,e^- \quad (m)$$

It can be concluded that a higher KOH concentration can not only increase the formation of Pd–OH_{ads} at lower potentials, but also accelerate dehydrogenation to facilitate the whole process. As a result, E_p shifts negatively with increasing KOH concentration. Interestingly, 1.0 M KOH appears to provide the most effective electrocatalytic performance for the synthesized Pd–MWNT-COOH nanocatalysts in the MOR. 12.0 M aqueous methanol fuel is observed to exhibit the highest j_p value due to the balanced coverage of adsorbed methanol and hydroxyl groups.

© 2015 Wiley-VCH Verlag GmbH & Co. KGaA, Weinheim

2.2.4. Effect of Temperature on Electrode Kinetics

Figure 10 shows the cyclic voltammograms of MOR on the Pd–MWNT-COOH electrode in 1.0 M KOH solution containing 1.0 M methanol at temperatures of 2, 22, and 40 °C with a scan rate of 50 mV s^{-1}. The electrode exhibited similar CV profiles at all

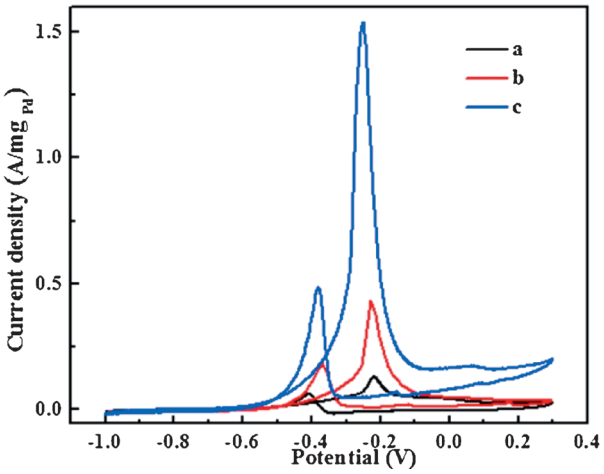

Figure 10. CV of the Pd–MWNT-COOH electrode in 1.0 M KOH containing 1.0 M methanol at 2, 22, and 40 °C, at a scan rate of 50 mV s^{-1}.

temperatures. The voltammograms display the same key features, such as the presence of a forward oxidation peak in the forward sweep, centered around −0.2 V, and the re-oxidation region in the reverse scan starting at approximately −0.3 V. An increased j_p value was observed with increasing temperature, as much as 12-fold higher as temperature is increased from 2 to 40 °C. In addition, a clear negative shift of onset potential with increasing temperature was observed, suggesting that the increased temperature has a positive effect on the MOR as expected. As OH^- adsorbs on the electrode surface more readily at higher temperatures,[63] the positive role of OH^- can not only facilitate dehydrogenation, but can also result in a lower onset potential, thus leading to an increased j_p value.

In order to further investigate the effect of temperature on the reaction kinetics, slow linear-sweep voltammetry (SLV) of Pd–MWNT-COOH was conducted in 1.0 M KOH containing 1.0 M methanol at 2, 22, and 40 °C (Figure 11 a). For all temperatures, the current densities were observed to increase slowly with increasing polarization potential in the low-potential region. The near overlap of all the three curves is ascribed to adsorbed hydrogen and water. However, in the relatively high-potential region, the polarization current increases sharply with polarization potential and reaches a limiting current at less than −0.25 V. The sharp increase is attributed to the oxidation of methanol and the current plateau is due to blocking of the Pd active catalytic sites by adsorbed CO_{ads} species. The oxidation of methanol starts more negatively at higher temperatures, implying an more favored oxidation of methanol with increasing temperature. In addition, the varying trends of current are also consistent with the CV results. Figure 11 b displays

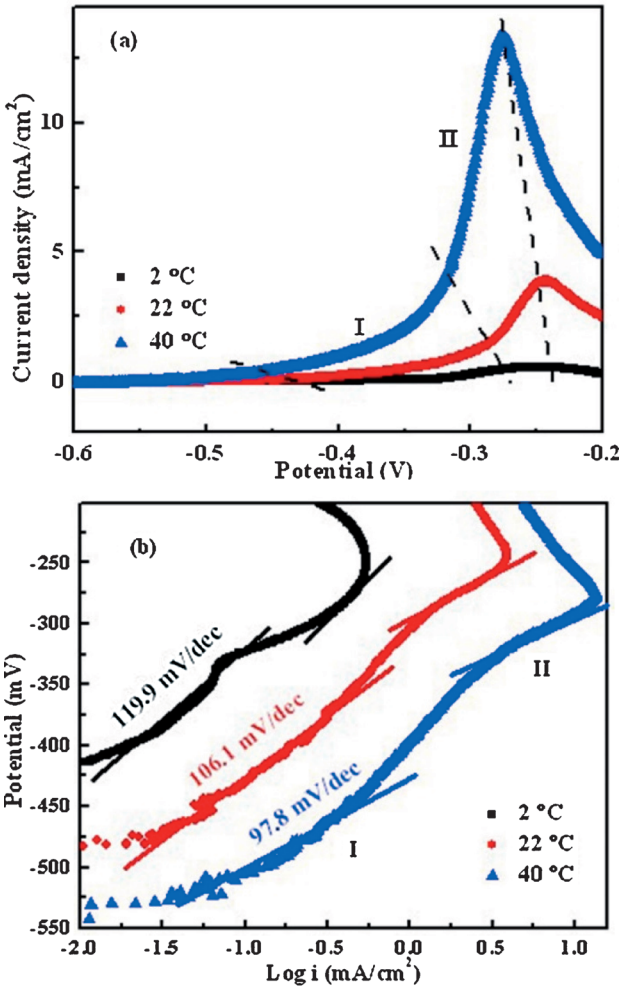

Figure 11. Tafel plots of the MOR at the Pd–MWNT-COOH electrode in 1.0 M KOH containing 1.0 M methanol at 2, 22, and 40 °C, at a scan rate of 0.5 mV s^{-1}.

Tafel plots for the anode polarization at the three temperatures. Each plot is mainly fitted and divided into two linear regions (I and II) according to the change of Tafel slopes, indicating a change in the methanol oxidation mechanism or a change in the dominant reactions.[64] The Tafel slope of approximately 110 mV dec^{-1} confirmed that splitting of the first C–H bond of CH_3OH molecules with the first electron transfer is the rate-determining step on Pd–MWNT-COOH in region I.[65] However, different Tafel slopes in region II reveal an alternative mechanism that the rate-determining step shifts from methanol dehydrogenation to CO_{ads} oxidation.[65] All the Tafel slopes in both ranges decrease slightly with increasing temperature, which implies an enhanced reaction rate. The enhanced reaction rate can be reasonably explained, in that an elevated temperature can not only activate the C–H bond scission, but can also accelerate the oxidation reaction of CO_{ads} species.[65,66]

The influence of temperature on the long-term stability of the Pd–MWNT-COOH electrode was also studied using CA (Figure 12). Typically, the potential chosen during the stability test is less than the peak potential. However, in this study the

© 2015 Wiley-VCH Verlag GmbH & Co. KGaA, Weinheim

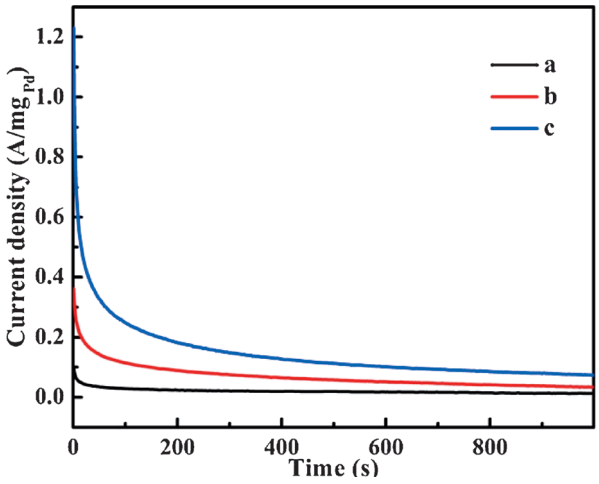

Figure 12. CA of the Pd–MWNT-COOH electrode in 1.0 M KOH containing 1.0 M methanol at 2, 22, and 40 °C, at a scan rate of 50 mV s^{-1}.

potential was initially set at the peak potential (−0.2 V) and the experiment was carried out at different temperatures over a period of 1000 s, with the aim of maintaining the highest oxidation speed in order to better justify the tolerance of the nanocatalysts towards poisoning species. It is clear that the extreme current density increases with the increase in temperature, as the current decay is mainly due to the poisoning effect of CO_{ads} species.[67] The poor catalyst tolerance at 2 °C is mainly due to the low rate of dehydrogenation and an accumulation of poisoning species. In contrast, the catalyst exhibits comparatively low decay of current density and reasonably high extreme current density at 40 °C, indicating that the electrode shows improved tolerance to the poisoning species at higher temperatures. Because the increasing reaction rate is related to the increase in the adsorption–dehydrogenation reaction step,[68] the increased stability can be attributed to the faster rate of dehydrogenation and the enhanced mobility of ions. In addition, the favorable adsorption of OH^- on the surface also greatly facilitates the dehydrogenation process and reaction with poisoning CO_{ads} species.[53]

3. Conclusions

The carboxyl-MWNT-stabilized Pd nanocatalysts were prepared using a facile one-pot solution-based thermal decomposition method. The Pd nanoparticles were uniformly distributed and strongly anchored onto the MWNT-COOH surface through their interaction with carboxyl groups. The electrochemical performance of the synthesized Pd–MWNT-COOH and Pd–MWNTs nanocatalysts in the MOR were much better than that of bare Pd nanoparticles, confirming the positive role of the MWNT support. The carboxyl groups were observed to be responsible for the evenly dispersed Pd nanoparticles and higher electrocatalytic activity. The effects of methanol, KOH concentration and temperature on the Pd–MWNT-COOH for the MOR were evaluated and an optimum peak current density was determined by means of balanced adsorption of methanol and hydroxide on the electrode surface. Two rate-determining steps—cleavage of the C–H bond and CO_{ads} oxidation—were found to be enhanced with increasing temperature, implying an improved electrocatalytic performance at a higher temperature.

Experimental Section

Materials

Palladium(II) acetylacetonate [$Pd(C_5H_7O_2)_2$, 99%] and methanol (anhydrous, ≥99.5%) were purchased from Sigma–Aldrich. Xylene (laboratory grade, $\rho = 0.87\ g\,cm^{-3}$) was purchased from Fisher Scientific. MWNTs (stock: 1233YJ, 50–80 nm diameter, 10–20 μm length, 95%, 40 $m^2\,g^{-1}$) and MWNT-COOH (stock: 1272YJF, 95%, COOH content: 0.47–0.51 wt%, 50–80 nm diameter, 10–20 μm length) were provided by Nanostructured and Amorphous Materials, Inc (Houston, TX). All the chemicals were used as received without further treatment.

Synthesis of Catalysts

A facile one-pot solution-based method was used to synthesize bare Pd NPs, Pd–MWNTs and Pd–MWNT-COOH. In brief, MWNTs or MWNT-COOH (100.0 mg) were dispersed in xylene (60 mL) in a 100 mL beaker with sonication for 1 h. The mixture was then transferred to a 250 mL three-neck flask and heated to reflux (≈140 °C) over approximately 20 min. A mixture of $Pd(acac)_2$ (304.0 mg) and xylene (20 mL) in a 50 mL beaker was sonicated for 10 min and was then added to the MWNTs or MWNT-COOH xylene solution at reflux. The mixture was then heated at reflux for an additional 3 h to complete the reaction. Finally, the solution was allowed to cool to room temperature, filtered under vacuum and rinsed with ethanol and acetone three times. For the synthesis of bare Pd NPs, sonicated $Pd(acac)_2$ solution in xylene (20 mL) was added to hot xylene (60 mL) at reflux and heated at reflux for 3 h. The bare Pd NPs were then collected by centrifugation and rinsed with ethanol and acetone three times. The final products (Pd–MWNT-COOH, Pd–MWNTs and Pd NPs) were collected after vacuum drying at 60 °C for 24 h.

Preparation of Catalyst Working Electrode

Prior to each experiment, the working glassy carbon electrode (3 mm diameter) was successively polished with 1.0 and 0.05 μm alumina powders on a microcloth wetted with doubly distilled water to produce an electrode with a mirror-like surface. For the preparation of a catalyst-coated electrode, catalyst (1.0 mg) was added to an ethanolic solution of Nafion (0.1 wt%, 1.0 mL), then the mixture was subjected to ultrasonication for 30 min to form a uniform suspension. The obtained suspension (5 μL) was dropped on the surface of the glassy carbon electrode. Finally, the resulting modified glassy carbon electrode was air-dried at room temperature.

Characterization

XRD analysis of the nanocatalysts was carried out on a Bruker D8 ADVANCE X-ray diffractometer equipped with a CuKα source ($\lambda = 0.154$ nm) at 40 kV and 30 mA. The 2θ angular region between 20° and 70° was investigated at a scan rate of 1° min^{-1}.

© 2015 Wiley-VCH Verlag GmbH & Co. KGaA, Weinheim

A transmission electron microscope (JEOL 2010F) was used to characterize the morphology of the prepared Pd nanocatalysts at a working voltage of 200 kV. The samples were prepared by drying a drop of ethanol suspension on a 400-mesh carbon-coated copper grid (Electron Microscopy Sciences, Hotfield, Pennsylvania).

Raman spectra were measured using a Horiba Jobin–Yvon LabRam Raman confocal microscope with 785 nm laser excitation at 1.5 cm^{-1} resolution at room temperature.

XPS measurements were performed on a Kratos AXIS 165 XPS/AES instrument. The samples were scanned with a monochromatic Al X-ray source, 10 kV anode potential, and beam current of 15 mA. The Pd peaks were deconvoluted into the components on a Shirley background.

TGA was conducted using a TA instruments Q-500 analyzer at a heating rate of 10 °C min^{-1} and an air flow rate of 60 mL min^{-1} from 30 to 700 °C.

Electrochemical Evaluation

The electrochemical experiments were conducted in a conventional three-electrode cell. The glassy carbon electrode deposited with catalyst was used as the working electrode, platinum wire as the counter electrode, and an SCE (0.241 V vs. SHE) connected to the cell through a Luggin capillary serving as reference electrode. All the potentials were referenced to the SCE.

CV was measured over the potential range −1.0–0.3 V at a sweep rate of 50 mV s^{-1} on a VersaSTAT4 potentiostat electrochemical workstation (Princeton Applied Research, Oak Ridge, Tennessee). Before all experiments, solvents were deaerated with N_2 for 10 min. The stable voltammogram curves were recorded after several potential extended cycles in the prepared electrolytes. For each particular temperature, a CA measurement was performed on the same electrode for 1000 s. The voltammetric and chronoamperometric currents were normalized to the electrochemically active Pd mass calculated from the TGA. EIS was carried out in the frequency range 0.1–100 000 Hz at 5 mV amplitude and at −0.4 V versus the reference electrode. Tafel polarization curves were obtained from the linear polarization curves from −0.8 to −0.2 V with a scan rate of 0.5 mV s^{-1}, and the current density was normalized to the area of coated nanocatalysts.

Acknowledgements

This project was supported by a Seeded Research Enhancement Grant (REG) from Lamar University. Partial financial support from the National Science Foundation Chemical and Biological Separations program (CBET: 11–37441), managed by Dr. Rosemarie D. Wesson is appreciated. We also appreciate the support from the National Science Foundation Nanoscale Interdisciplinary Research Team and Materials Processing and Manufacturing (CMMI 10–30755) USA to fund TGA.

Keywords: carbon nanotubes · concentration and temperature effects · electrocatalysis · methanol oxidation · palladium

[1] a) T. Teranishi, M. Miyake, *Chem. Mater.* **1999**, *11*, 3414–3416; b) X. Huang, S. Tang, X. Mu, Y. Dai, G. Chen, Z. Zhou, F. Ruan, Z. Yang, N. Zheng, *Nat. Nanotechnol.* **2011**, *6*, 28–32.
[2] J. Li, A. Staykov, T. Ishihara, K. Yoshizawa, *J. Phys. Chem. C* **2011**, *115*, 7392–7398.
[3] a) Y. Mizukoshi, K. Okitsu, Y. Maeda, T. A. Yamamoto, R. Oshima, Y. Nagata, *J. Phys. Chem. B* **1997**, *101*, 7033–7037; b) S. Giorgio, C. Chapon, C. R. Henry, *Langmuir* **1997**, *13*, 2279–2284.
[4] a) B. Lim, M. Jiang, J. Tao, P. H. C. Camargo, Y. Zhu, Y. Xia, *Adv. Funct. Mater.* **2009**, *19*, 189–200; b) Q. Yuan, Z. Zhou, J. Zhuang, X. Wang, *Chem. Commun.* **2010**, *46*, 1491–1493.
[5] a) Y. Xiong, H. Cai, B. J. Wiley, J. Wang, M. J. Kim, Y. Xia, *J. Am. Chem. Soc.* **2007**, *129*, 3665–3675; b) Y. H. Chen, H. H. Hung, M. H. Huang, *J. Am. Chem. Soc.* **2009**, *131*, 9114–9121.
[6] a) X. Huang, N. Zheng, *J. Am. Chem. Soc.* **2009**, *131*, 4602–4603; b) H.-W. Liang, S. Liu, J.-Y. Gong, S.-B. Wang, L. Wang, S.-H. Yu, *Adv. Mater.* **2009**, *21*, 1850–1854.
[7] X. Huang, S. Tang, H. Zhang, Z. Zhou, N. Zheng, *J. Am. Chem. Soc.* **2009**, *131*, 13916–13917.
[8] W. Niu, L. Zhang, G. Xu, *ACS Nano* **2010**, *4*, 1987–1996.
[9] J. Watt, S. Cheong, M. F. Toney, B. Ingham, J. Cookson, P. T. Bishop, R. D. Tilley, *ACS Nano* **2010**, *4*, 396–402.
[10] H. Bai, M. Han, Y. Du, J. Bao, Z. Dai, *Chem. Commun.* **2010**, *46*, 1739–1741.
[11] N. Tian, Z. Y. Zhou, N. F. Yu, L. Y. Wang, S. G. Sun, *J. Am. Chem. Soc.* **2010**, *132*, 7580–7581.
[12] Y. Fang, S. Guo, C. Zhu, S. Dong, E. Wang, *Langmuir* **2010**, *26*, 17816–17820.
[13] a) J. H. Byeon, Y.-W. Kim, *ACS Appl. Mater. Interfaces* **2011**, *3*, 2912–2918; b) X. Ren, P. Zelenay, S. Thomas, J. Davey, S. Gottesfeld, *J. Power Sources* **2000**, *86*, 111–116.
[14] C. Xu, L. Cheng, P. Shen, Y. Liu, *Electrochem. Commun.* **2007**, *9*, 997–1001.
[15] R. N. Singh, A. Singh Anindita, *Int. J. Hydrogen Energy* **2009**, *34*, 2052–2057.
[16] Z. J. Mellinger, T. G. Kelly, J. G. Chen, *ACS Catal.* **2012**, *2*, 751–758.
[17] a) X. Chen, Y. Hou, H. Wang, Y. Cao, J. He, *J. Phys. Chem. C* **2008**, *112*, 8172–8176; b) M. Zhao, L. Sun, R. M. Crooks, *J. Am. Chem. Soc.* **1998**, *120*, 4877–4878.
[18] H. Sakurai, T. Tsukuda, T. Hirao, *J. Org. Chem.* **2002**, *67*, 2721–2722.
[19] L. S. Zhong, J. S. Hu, Z. M. Cui, L. J. Wan, W. G. Song, *Chem. Mater.* **2007**, *19*, 4557–4562.
[20] K. Mori, K. Yamaguchi, T. Hara, T. Mizugaki, K. Ebitani, K. Kaneda, *J. Am. Chem. Soc.* **2002**, *124*, 11572–11573.
[21] V. G. Pol, H. Grisaru, A. Gedanken, *Langmuir* **2005**, *21*, 3635–3640.
[22] K. Ding, H. Jia, S. Wei, Z. Guo, *Ind. Eng. Chem. Res.* **2011**, *50*, 7077–7082.
[23] J. Kim, G. W. Roberts, D. J. Kiserow, *Chem. Mater.* **2006**, *18*, 4710–4712.
[24] B. Astinchap, R. Moradian, A. Ardu, C. Cannas, G. Varvaro, A. Capobianchi, *Chem. Mater.* **2012**, *24*, 3393–3400.
[25] J. Kong, M. G. Chapline, H. Dai, *Adv. Mater.* **2001**, *13*, 1384–1386.
[26] a) D. Bera, S. C. Kuiry, M. McCutchen, S. Seal, H. Heinrich, G. C. Slane, *J. Appl. Phys.* **2004**, *96*, 5152–5157; b) D.-d. Zhou, L. Ding, H. Cui, H. An, J.-p. Zhai, Q. Li, *Chem. Eng. J.* **2012**, *200*, 32–38; c) X. R. Ye, Y. Lin, C. M. Wai, *Chem. Commun.* **2003**, 642–643; d) X. R. Ye, Y. Lin, C. Wang, M. H. Engelhard, Y. Wang, C. M. Wai, *J. Mater. Chem.* **2004**, *14*, 908–913; e) Y. Lin, X. Cui, C. Yen, C. M. Wai, *J. Phys. Chem. B* **2005**, *109*, 14410–14415.
[27] a) J. P. Tessonnier, L. Pesant, G. Ehret, M. J. Ledoux, C. Pham-Huu, *Appl. Catal. A* **2005**, *288*, 203–210; b) S.-u. Rather, R. Zacharia, S. W. Hwang, K. S. Nahm, *Chem. Phys. Lett.* **2007**, *441*, 261–267.
[28] F. Yang, Y. Li, T. Liu, K. Xu, L. Zhang, C. Xu, J. Gao, *Chem. Eng. J.* **2013**, *226*, 52–58.
[29] a) X. Ji, C. E. Banks, A. F. Holloway, K. Jurkschat, C. A. Thorogood, G. G. Wildgoose, R. G. Compton, *Electroanalysis* **2006**, *18*, 2481–2485; b) U. Schlecht, K. Balasubramanian, M. Burghard, K. Kern, *Appl. Surf. Sci.* **2007**, *253*, 8394–8397; c) S. Mubeen, T. Zhang, B. Yoo, M. A. Deshusses, N. V. Myung, *J. Phys. Chem. C* **2007**, *111*, 6321–6327; d) A. D. Franklin, J. T. Smith, T. Sands, T. S. Fisher, K.-S. Choi, D. B. Janes, *J. Phys. Chem. C* **2007**, *111*, 13756–13762; e) T. M. Day, P. R. Unwin, J. V. Macpherson, *Nano Lett.* **2007**, *7*, 51–57; f) D. J. Guo, H. L. Li, *Electrochem. Commun.* **2004**, *6*, 999–1003.

© 2015 Wiley-VCH Verlag GmbH & Co. KGaA, Weinheim

[30] a) V. Georgakilas, D. Gournis, V. Tzitzios, L. Pasquato, D. M. Guldi, M. Prato, *J. Mater. Chem.* **2007**, *17*, 2679 – 2694; b) V. Lordi, N. Yao, J. Wei, *Chem. Mater.* **2001**, *13*, 733 – 737; c) M. S. Raghuveer, S. Agrawal, N. Bishop, G. Ramanath, *Chem. Mater.* **2006**, *18*, 1390 – 1393; d) R. Yu, L. Chen, Q. Liu, J. Lin, K.-L. Tan, S. C. Ng, H. S. O. Chan, G.-Q. Xu, T. S. A. Hor, *Chem. Mater.* **1998**, *10*, 718 – 722.
[31] a) W. Daniell, H. Landes, N. E. Fouad, H. Knözinger, *J. Mol. Catal. A* **2002**, *178*, 211 – 218; b) K. Esumi, T. Tano, K. Meguro, *Langmuir* **1989**, *5*, 268 – 270; c) N. Mahata, V. Vishwanathan, *J. Catal.* **2000**, *196*, 262 – 270; d) Z. Yin, H. Zheng, D. Ma, X. Bao, *J. Phys. Chem. C* **2009**, *113*, 1001 – 1005.
[32] V. Mazumder, S. Sun, *J. Am. Chem. Soc.* **2009**, *131*, 4588 – 4589.
[33] a) T. Teranishi, M. Miyake, *Chem. Mater.* **1998**, *10*, 594 – 600; b) A. Nemamcha, J.-L. Rehspringer, D. Khatmi, *J. Phys. Chem. B* **2006**, *110*, 383 – 387.
[34] S. Kundu, Y. M. Wang, W. Xia, M. Muhler, *J. Phys. Chem. C* **2008**, *112*, 16869 – 16878..
[35] U. Schlotterbeck, C. Aymonier, R. Thomann, H. Hofmeister, M. Tromp, W. Richtering, S. Mecking, *Adv. Funct. Mater.* **2004**, *14*, 999 – 1004.
[36] M. A. Pimenta, G. Dresselhaus, M. S. Dresselhaus, L. G. Cancado, A. Jorio, R. Saito, *Phys. Chem. Chem. Phys.* **2007**, *9*, 1276 – 1290.
[37] a) C. Furtado, U. Kim, H. Gutierrez, L. Pan, E. Dickey, P. C. Eklund, *J. Am. Chem. Soc.* **2004**, *126*, 6095 – 6105; b) U. J. Kim, C. A. Furtado, X. Liu, G. Chen, P. C. Eklund, *J. Am. Chem. Soc.* **2005**, *127*, 15437 – 15445.
[38] a) H. Telg, M. Fouquet, J. Maultzsch, Y. Wu, B. Chandra, J. Hone, T. F. Heinz, C. Thomsen, *Phys. Status Solidi B* **2008**, *245*, 2189 – 2192; b) S. Piscanec, M. Lazzeri, J. Robertson, A. C. Ferrari, F. Mauri, *Phys. Rev. B* **2007**, *75*, 035427.
[39] V. Datsyuk, M. Kalyva, K. Papagelis, J. Parthenios, D. Tasis, A. Siokou, I. Kallitsis, C. Galiotis, *Carbon* **2008**, *46*, 833 – 840.
[40] B. Olalde, J. M. Aizpurua, A. García, I. Bustero, I. Obieta, M. a. J. Jurado, *J. Phys. Chem. C* **2008**, *112*, 10663 – 10667.
[41] M. E. Rincón, M. E. Trujillo-Camacho, M. Miranda-Hernández, A. K. Cuentas-Gallegos, G. Oromo, *J. Nanosci. Nanotechnol.* **2007**, *7*, 1596 – 1603.
[42] X. Yang, M. Zhen, G. Li, X. Liu, X. Wang, C. Shu, L. Jiang, C. Wang, *J. Mater. Chem. A* **2013**, *1*, 8105 – 8110.
[43] a) H. Lin, J. Yang, J. Liu, Y. Huang, J. Xiao, X. Zhang, *Electrochim. Acta* **2013**, *90*, 382 – 392; b) M. Brun, A. Berthet, J. Bertolini, *J. Electron Spectrosc. Relat. Phenom.* **1999**, *104*, 55 – 60.
[44] T. Pillo, R. Zimmermann, P. Steiner, S. Hüfner, *J. Phys. Condens. Matter* **1997**, *9*, 3987.
[45] N. Kakati, J. Maiti, S. H. Lee, Y. S. Yoon, *Int. J. Hydrogen Energy* **2012**, *37*, 19055 – 19064.
[46] Y. Li, W. Zhou, H. Wang, L. Xie, Y. Liang, F. Wei, J. C. Idrobo, S. J. Pennycook, H. Dai, *Nat. Nanotechnol.* **2012**, *7*, 394 – 400.
[47] S. Santra, P. Ranjan, P. Bera, P. Ghosh, S. K. Mandal, *RSC Adv.* **2012**, *2*, 7523 – 7533.
[48] a) S.-W. Kim, J. Park, Y. Jang, Y. Chung, S. Hwang, T. Hyeon, Y. W. Kim, *Nano Lett.* **2003**, *3*, 1289 – 1291; b) J. V. Hoene, R. G. Charles, W. M. Hickam, *J. Phys. Chem.* **1958**, *62*, 1098 – 1101.
[49] H. Huang, X. Wang, *J. Mater. Chem.* **2012**, *22*, 22533 – 22541.
[50] a) Z. X. Liang, T. S. Zhao, J. B. Xu, L. D. Zhu, *Electrochim. Acta* **2009**, *54*, 2203 – 2208; b) R. Awasthi, R. N. Singh, *Catal. Sci. Technol.* **2012**, *2*, 2428 – 2432.
[51] Z. S. Yang, J. J. Wu, *Fuel Cells* **2012**, *12*, 420 – 425.
[52] J. Z. Sun, Y. Z. Wang, C. Zhang, T. Y. Kou, Z. H. Zhang, *Electrochem. Commun.* **2012**, *21*, 42 – 45.
[53] S. S. Mahapatra, A. Dutta, J. Datta, *Int. J. Hydrogen Energy* **2011**, *36*, 14873 – 14883.
[54] T. H. Madden, E. M. Stuve, *J. Electrochem. Soc.* **2003**, *150*, E571 – E577.
[55] S. L. Gojković, T. R. Vidaković, D. R. Durović, *Electrochim. Acta* **2003**, *48*, 3607 – 3614.
[56] Y. Zhang, H. Shu, G. Chang, K. Ji, M. Oyama, X. Liu, Y. He, *Electrochim. Acta* **2013**, *109*, 570 – 576.
[57] a) Q. He, W. Chen, S. Mukerjee, S. Chen, F. Laufek, *J. Power Sources* **2009**, *187*, 298 – 304; b) Y. Bai, J. Wu, J. Xi, J. Wang, W. Zhu, L. Chen, X. Qiu, *Electrochem. Commun.* **2005**, *7*, 1087 – 1090.
[58] J. J. Wang, G. P. Yin, J. Zhang, Z. B. Wang, Y. Z. Gao, *Electrochim. Acta* **2007**, *52*, 7042 – 7050.
[59] Y. Lin, X. Cui, C. H. Yen, C. M. Wai, *Langmuir* **2005**, *21*, 11474 – 11479.
[60] C. C. Yang, T. Wu, H. R. Chen, T. H. Hsieh, K. S. Ho, C. W. Kuo, *Int. J. Electrochem. Sci.* **2011**, *6*, 1642.
[61] L. A. Estudillo-Wong, A. M. Vargas-Gómez, E. M. Arce-Estrada, A. Manzo-Robledo, *Electrochim. Acta* **2013**, *112*, 164 – 170.
[62] M. A. Abdel Rahim, R. M. Abdel Hameed, M. Khalil, *J. Power Sources* **2004**, *134*, 160 – 169.
[63] J.-H. Choi, K.-W. Park, B.-K. Kwon, Y.-E. Sung, *J. Electrochem. Soc.* **2003**, *150*, A973 – A978.
[64] G. Wu, L. Li, B. Q. Xu, *Electrochim. Acta* **2004**, *50*, 1 – 10.
[65] J. Zhu, F. Cheng, Z. Tao, J. Chen, *J. Phys. Chem. C* **2008**, *112*, 6337 – 6345.
[66] L. Dubau, C. Coutanceau, E. Garnier, J. M. Léger, C. Lamy, *J. Appl. Electrochem.* **2003**, *33*, 419 – 429.
[67] Z. Liu, X. Zhang, L. Hong, *Electrochem. Commun.* **2009**, *11*, 925 – 928.
[68] A. V. Tripković, K. D. Popović, B. N. Grgur, B. Blizanac, P. N. Ross, N. M. Marković, *Electrochim. Acta* **2002**, *47*, 3707 – 3714.

Received: November 8, 2014
Published online on January 23, 2015

© 2015 Wiley-VCH Verlag GmbH & Co. KGaA, Weinheim